SCIENTIFIC REP🔾RTS

OPEN

Metallic Sn spheres and SnO$_2$@C core-shells by anaerobic and aerobic catalytic ethanol and CO oxidation reactions over SnO$_2$ nanoparticles

Won Joo Kim[1], Sung Woo Lee[2] & Youngku Sohn[1]

SnO$_2$ has been studied intensely for applications to sensors, Li-ion batteries and solar cells. Despite this, comparatively little attention has been paid to the changes in morphology and crystal phase that occur on the metal oxide surface during chemical reactions. This paper reports anaerobic and aerobic ethanol and CO oxidation reactions over SnO$_2$ nanoparticles (NPs), as well as the subsequent changes in the nature of the NPs. Uniform SnO$_2$@C core-shells (10 nm) were formed by an aerobic ethanol oxidation reaction over SnO$_2$ NPs. On the other hand, metallic Sn spheres were produced by an anaerobic ethanol oxidation reaction at 450 °C, which is significantly lower than that (1200 °C) used in industrial Sn production. Anaerobic and aerobic CO oxidation reactions were also examined. The novelty of the methods for the production of metallic Sn and SnO$_2$@C core-shells including other anaerobic and aerobic reactions will contribute significantly to Sn and SnO$_2$-based applications.

Tin (IV) oxide (SnO$_2$) has been studied widely because of its potential applicability to lithium-ion batteries, gas-sensors, solar cells, and catalysts[1–3]. Considerable efforts have been made to control the exposed crystal facets, and synthesize pure and hybridized SnO$_2$ materials with a range of morphologies, including hollow nanoparticles, wires, nanorods, nanotubes, nanoparticles, nanosheets, and cubes[4–16]. C/SnO$_2$ hybrid materials were reported to have potential applicability to Li-ion batteries[17–22]. Recently, Liang et al. synthesized bowl-like SnO$_2$@C hollow nanoparticles to retain the advantages of hollow structures, and showed high performance as an anode material for Li-ion batteries[17]. The SnO$_2$ materials reported for applications to Li-ion batteries include hollow SnO$_2$[23], SnO$_2$ nanotubes[9,24], nanosheets[12,25], nanoboxes[26], NiCo$_2$O$_4$@SnO$_2$ hetero-nanostructures[27], capped Sn/SnO$_2$ nanocrystals[28], sandwich-stacked SnO$_2$/Cu nanosheets[29], graphene/SnO$_2$ nanoribbon composites[30], and SnO$_2$@TiO$_2$ core-shells[31], Gas-sensing is an active research area for SnO$_2$ nanomaterials[32–47]. A wide range of materials have been prepared and tested as sensor materials. These include Cu-doped SnO$_2$ film for H$_2$S sensing[33], multi-layer SnO$_2$ nanoplates[34] and flower-like SnO$_2$ for ethanol sensing[35], aligned epitaxial SnO$_2$ nanowires for ppb-level NO$_2$ sensing[36], p-Te/n-SnO$_2$ hierarchical heterostructures[37] and SnO$_2$ hollow spheres for ppm-level CO sensing[38], hollow SnO$_2$ nanofibers[39] and graphene/SnO$_2$ hybrids[40] for H$_2$ sensing, clustered SnO$_2$ NPs for toluene detection[41], and SnO$_2$ NP-coated ZnO nanotubes for electrochemical dopamine sensing[42], For solar cell applications[48–51], Dong et al. reported that quintuple-shelled SnO$_2$ hollow microspheres showed superior light scattering suitable for dye-sensitized solar cells[50]. The (thermal and photo) catalytic activity of SnO$_2$ has also been studied actively[52–57]. Several examples include the inactivation of bacteria using fluorinated

[1]School of Chemistry and Biochemistry, Yeungnam University, Gyeongsan 38541, Republic of Korea. [2]Center for Research Facilities & Department of Materials Science and Engineering, Chungnam National University, Daejeon 34134, Republic of Korea. Correspondence and requests for materials should be addressed to Y.S. (email: youngkusohn@ynu.ac.kr)

SnO_2 hollow nanospheres[52], rhodamine B treatment using flower-like hollow SnO/Sn_3O_4 microspheres[53], Rhodamine 6G photodegradation using hollow supersymmetric SnO_2 microspheres[54]. SnO_2 nanorods with exposed (110) facets were reported to have high CO oxidation activity following a Mars–van Krevelen mechanism, even though the nanorods have a low surface area and a less active surface oxygen species[55,56]. Studying the surface reaction on SnO_2 is extremely important to better understand the sensing and catalytic mechanism and for fabricating the nanostructures. Adsorption is a common first step for both sensing and catalytic reactions. Jeong *et al.* reported that nanotextured SnO_2 surfaces could be produced using a self-catalytic growth method with different oxygen concentrations and annealing temperatures[58]. Müller *et al.* reported showed that the precursor chemistry was important for controlling the morphology and composition of SnO_2 nanowires[59].

The specific aim of this study was to identify the changes in morphology and crystal phase of SnO_2 NPs after aerobic and anaerobic oxidation reactions. This paper reports a new methodology for the production of metallic Sn spheres and SnO_2@C core-shells. The core-shell structures have very high potential applicability to gas sensing and Li-ion batteries. Metallic Sn spheres were produced from SnO_2 by an anaerobic ethanol oxidation reaction below 600 °C, which is a significantly lower temperature than that used in the high temperature (>1000 °C) carbothermal reduction method in industry. In addition, the high CO oxidation activity of SnO_2 NPs has potential applications to catalysis.

Methods

SnO_2 NPs were synthesized using a facial hydrothermal method. Briefly, 10.0 mL of 0.1 M $SnCl_4 \cdot 5H_2O$ and 20 mL of deionized water (18.2 MΩ-cm resistivity) were fully mixed in a Teflon bottle. An appropriate amount of 0.1 M NaOH solution was then added to induce precipitation. The bottle was tightly capped and placed in an oven at 120 °C for 12 hours. The reaction bottle was cooled naturally and the white precipitate was collected by centrifugation. The precipitates were washed several times with deionized water and ethanol, and dried in an ambient oven at 70 °C. The morphology and size of the dried powder samples were examined by transmission electron microscopy (TEM, Hitachi H-7600) operated at 100.0 kV. A high resolution TEM image was obtained using a FEI Tecnai G2 F20 S-TWIN at an applied voltage of 200.0 kV. The surface morphology and the chemical composition were examined by scanning electron microscopy (SEM) and energy dispersive X-ray (EDX) analysis, respectively using a Hitachi S-4100 SEM/EDX. The X-ray diffraction (XRD) patterns for the powder samples were obtained using a PANalytical X'Pert Pro MPD diffractometer using Cu Kα radiation. The crystal structures of the metallic Sn spheres were tested by both powder and single crystal X-ray diffraction experiments. Powder X-ray diffraction was conducted using a Bruker AXS D8 diffractometer with a Cu Kα radiation source (40 kV and 40 mA) using a Linxeye 1-D detector. Single crystal X-ray diffraction was conducted using a Bruker AXS APEX II CCD-single crystal diffractometer with a Mo Kα radiation source (50 kV and 30 mA, point beam) and a CCD detector system. The diffuse reflectance absorption spectra for the powder samples were measured using a double beam Neosys-2000 UV–Vis spectrophotometer (Scinco). X-ray photoelectron spectroscopy (XPS) was performed using a Thermo-VG Scientific MultiLab 2000 with a monochromatic Al Kα X-ray source (1486.6 eV) equipped with a hemispherical energy analyzer. The photoluminescence spectra were obtained using a SCINCO (Seoul, South Korea) FluoroMate FS-2 spectrometer. Raman spectra were obtained using a Bruker Senterra Raman spectrometer at an excitation laser wavelength of 532 nm. The attenuated total reflection (ATR) Fourier transform infrared (FTIR) spectra were obtained using a Thermo scientific Nicolet iS10 spectrometer. The Brunauer-Emmett-Teller (BET) surface areas of the as-prepared powder samples were measured using a Quantachrome ChemBET TPR/TPD analyzer equipped with a thermal conductivity detector. Fig. S1 in the Supporting Information presents the schematics of the experimental setup for aerobic and anaerobic oxidation reactions. Briefly, for aerobic ethanol oxidation reaction, ethanol vapor was introduced into the catalyst by flowing 5% O_2/N_2 gas at a flow rate of 40 mL/min. Pure N_2 gas was used for the anaerobic ethanol oxidation reaction. The reaction products were examined using a SRS RGA200 quadrupole mass spectrometer. The temperature-programmed aerobic CO oxidation experiments were performed by flowing (40 mL/min) a CO (1%) and O_2 (2.5%) in N_2 gas mixture to the catalyst powder sample. For anaerobic CO oxidation, 5% CO/N_2 gas was flowed instead. The sample (20 mg) was placed in a U-quartz tube (4 mm inner diameter) for each oxidation experiment.

Results and Discussion.

Figure 1 shows a photograph and optical microscopy images of the samples produced after the ethanol oxidation reaction under aerobic (with O_2) and anaerobic (without O_2) conditions. The morphology changed significantly after the reactions. Upon the ethanol oxidation reaction under aerobic conditions, the white powder sample changed to a black powder. Interestingly, under anaerobic conditions, all the power samples changed to silvery-white spheres, indicating complete reduction to Sn metal. Several of the spheres were a few mm in size. To clearly show the metallic Sn spheres, a larger photograph is supplied in the Supporting information, Fig. S2.

Figure 2 presents the XRD patterns of the SnO_2 NPs before and after the aerobic ethanol oxidation reaction. All XRD peaks matched the standard crystal planes of tetragonal SnO_2 (JCPDS 1–0657), as displayed in Fig. 2. SnO_2 was likely obtained via $Sn^{4+} + OH^- \rightarrow$ Sn hydroxides $\rightarrow SnO_2 + H_2O$ during the hydrothermal reaction[10,15]. The three major XRD peaks at 2θ = 26.5, 33.8 and 51.7° were assigned to the (110), (101), and (211) reflection planes of tetragonal SnO_2, respectively. The XRD peaks of the
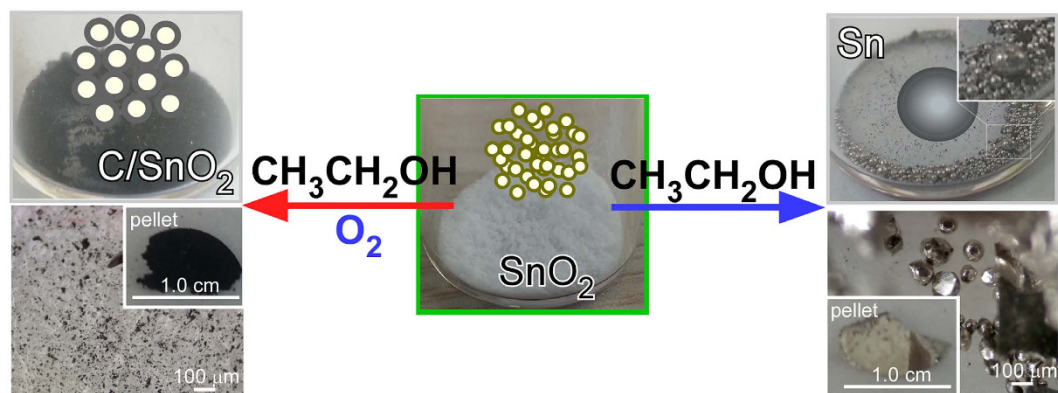
Figure 1. Photograph (top) and optical microscopy (bottom) images for the production of SnO₂@C core-shells (left, black in color) and metallic Sn spheres (right, silvery-white in color) by aerobic (left) and anaerobic (right) ethanol oxidation reactions over SnO₂ NPs (middle, white in color), respectively. The insets (left and right bottom two) in the optical microscopy images show photographs of the corresponding pelletized samples.
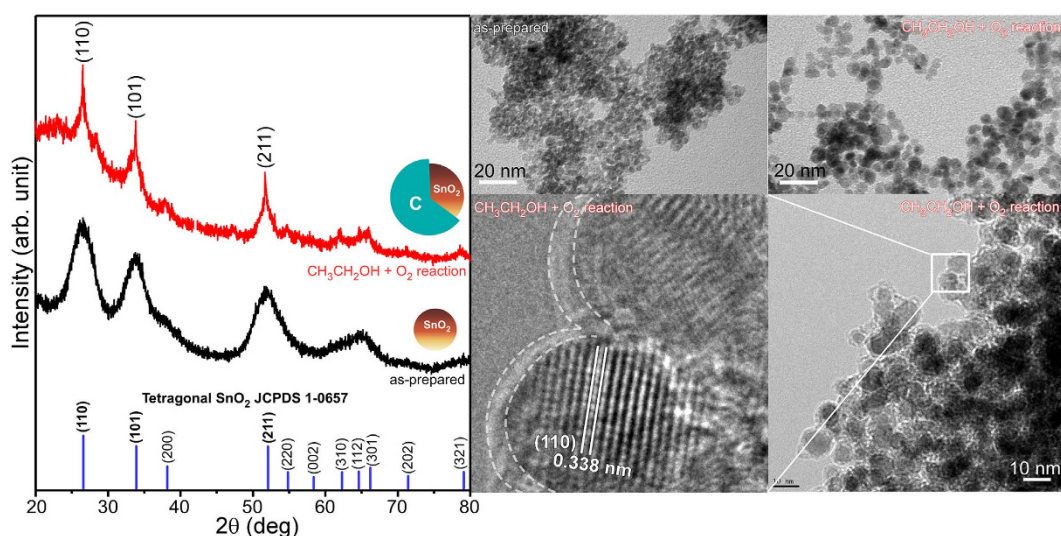

Figure 2. XRD patterns (left) and TEM/HRTEM (right) images of SnO₂ NPs before and after the aerobic ethanol oxidation reaction. The SnO₂@C core-shells were formed upon the aerobic reaction.

as-prepared sample were quite broad, indicating smaller particle sizes. The NP size was estimated using the Scherer formula, $d = K\lambda/L\cos\theta$, where K is the Scherer constant and L is the full width at half maximum of a reflection. The calculated particle size was in good agreement with the mean size (~2 nm) obtained from the TEM images. Li *et al.* also employed a similar hydrothermal (180 °C for 24 hrs) method to synthesize SnO₂ with reaction recipes of 1.0 mmol SnCl₄·5H₂O, 20 mL deionized water, 10 mL NaOH (1.5 M) solution, and 10 ML ethanol[60]. They obtained nanoparticle-aggregated hierarchical SnO₂ hollow microspheres (600–900 nm) and understood by dissolution–recrystallization process[60,61] with two major controlling factors of pH and reaction temperature.

For the SnO₂@C core-shells, the XRD peak became sharper, indicating an increase in crystallinity and/ or particle size. The TEM images illustrate the high uniformity and size of the SnO₂ NPs before and after the aerobic ethanol oxidation reaction. A clear lattice spacing of 3.38 Å was obtained, which is indicative of the single crystal nature. The spacing corresponds to the distance between the adjacent (110) planes of tetragonal SnO₂[25,30]. Alaf *et al.* and Uysal *et al.* employed an alternative method to obtain core-shell type structures, which were tested as anode materials for Li-ion batteries[62–64]. They thermal-evaporated metallic Sn on multiwalled carbon nanotube (MWCNT), and obtained Sn/SnO₂/MWCNT and Sn/MWCNT nanocomposites with and without plasma oxidation treatment, respectively. The grain sizes of Sn and SnO₂ were controlled by varying thermal evaporation and plasma oxidation conditions.

The as-prepared SnO₂ NPs were characterized by UV-Vis absorption spectroscopy, photoluminescence spectroscopy, FT-IR spectroscopy, and BET surface area measurements. A direct band gap of 3.4 eV was
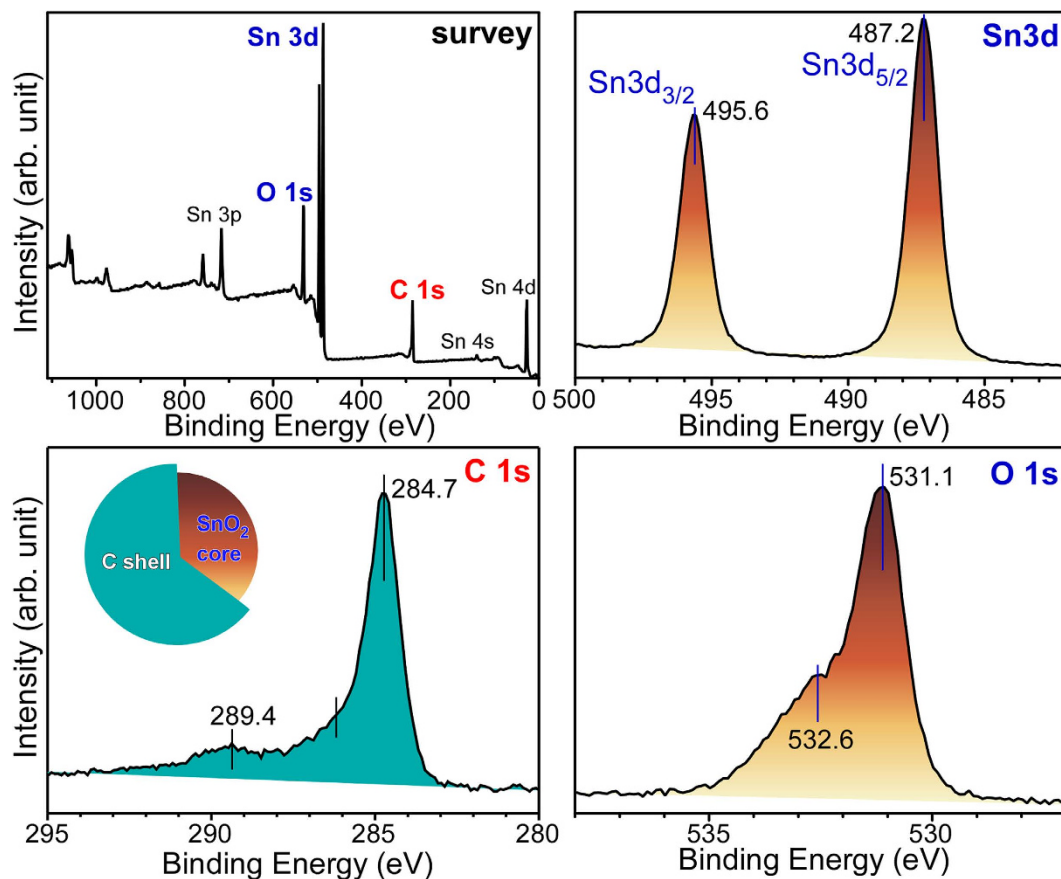
Figure 3. Survey (top left) and high resolution XP spectra of Sn 3d, C 1s and O 1s regions for SnO$_2$@C core-shells prepared by an aerobic ethanol oxidation reaction over SnO$_2$ NPs.

measured from the reflectance absorption spectrum and a plot of $(\alpha h\nu)^2$ versus hν (Supporting Info. Fig. S3)[53]. The photoluminescence spectrum was recorded for the as-prepared SnO$_2$ NPs at an excitation wavelength of 285 nm (Supporting Info. Fig. S4). Broad emission peaks were observed between 350 and 600 nm, which have commonly been attributed to oxygen defects (or vacancies)[45,65,66]. The as-prepared SnO$_2$ NPs exhibited a large amount of adsorbed water, based on the broad FT-IR peak at 3400 cm^{-1} (Supporting Info. Fig. S5)[38]. The broad peak was almost completely diminished after the aerobic ethanol oxidation reaction at temperatures up to 600 °C. The SnO$_2$ NPs (~2 nm) showed a BET surface area of 197.5 m^2/g, which is significantly larger than the surface area of 38.3 m^2/g for a reference ($>$100 nm, Sigma-Aldrich) SnO$_2$ powder. For comparison, Xi *et al.*[5] and Wang *et al.*[25] reported surface areas of 191.5 m^2/g for ultra-small (2nm) SnO$_2$ nanorods and 180.3 m^2/g for SnO$_2$ nanosheets, respectively.

The X-ray photoelectron spectra (Fig. 3) were recorded to further examine the chemical nature of the SnO$_2$@C core-shell nanostructures. The survey spectrum revealed the chemical information of Sn, O and carbon with no other elements. The prominent Sn 3d$_{3/2}$ and Sn 3d$_{5/2}$ XPS peaks were observed at 487.2 ($\pm$0.1) eV and 495.6 ($\pm$0.1) eV, respectively, with spin-orbit splitting of 8.4 eV, due to the Sn^{4+} oxidation state of SnO$_2$[14,31,55]. These binding energies (BEs) showed no critical difference from those of the as-prepared SnO$_2$ nanoparticles. This suggests that the overlayer carbon had been physisorbed on the SiO$_2$ surface. A major C 1s XPS peak was observed at 284.7 eV, due to elemental carbon. The two smaller C 1s peaks at 289.4 and 286 eV were assigned to O=C-O and C-OH/C-O-C species, respectively. These chemical species are related to the formation of ethylacetate and aldehyde after the aerobic ethanol oxidation reaction, as further discussed in detail below. Two O 1s XPS peaks were observed at 531.1 and 532.6 eV due to lattice oxygen (O^{2-}) of SnO$_2$ and adsorbed oxygen (O$^-$ abd O$_2^-$) species (e.g., H$_2$O and OH), respectively[14]. The adsorbed oxygen species were confirmed by FT-IR spectroscopy (Supporting Information, Fig. S5). The thickness of the carbon overlayer was estimated using a well-known equation[67], $I = I_0 \exp(-d/\lambda)$, where d is the shell thickness, λ is the electron inelastic mean-free path (IMFP)[68], I and I_o is the Sn 3d XPS intensities before and after carbon shell formation, respectively. The thickness of the carbon overlayer was calculated to be 1.2 nm using an IMFP (λ) of 2.7 nm[68].

The SnO$_2$@C core-shells were briefly tested as an oxygen sensor material (Supporting Info. Fig. S6) using a two-point probe resistance measurement method[43]. Using a SnO$_2$@C pellet, a surface resistance of 6 kΩ was measured at room temperature, which is an extremely low resistance compared to that of
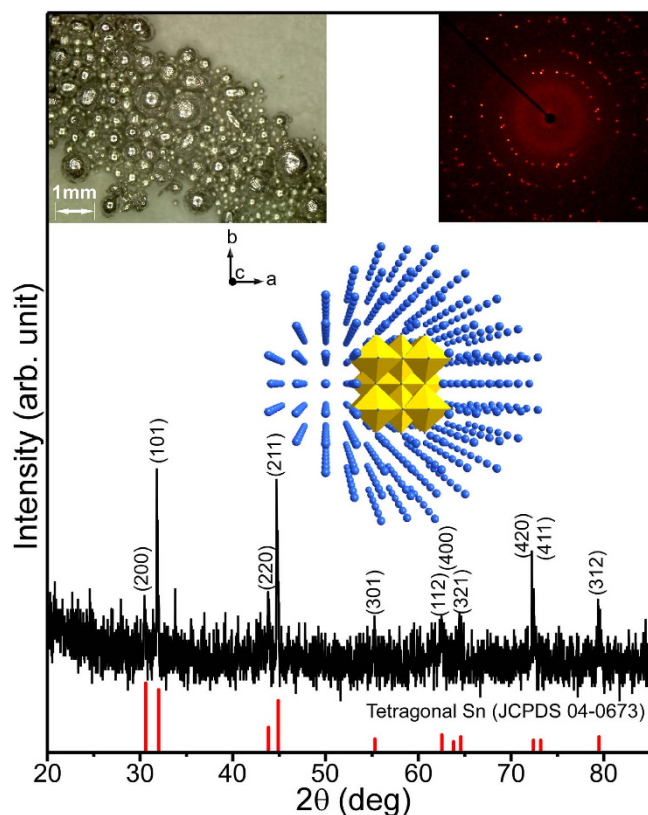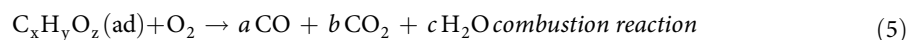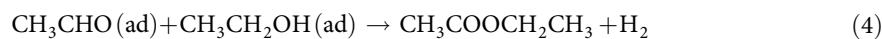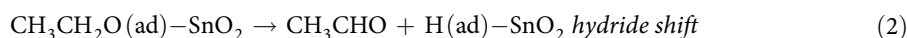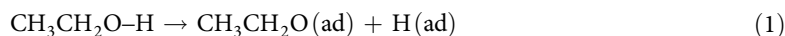
Figure 4. XRD patterns of metallic Sn formed by the anaerobic ethanol oxidation reaction. Optical microscopy image (top left inset), body centered tetragonal Sn crystal structure (middle inset), and crystal pattern of Phi 360 image (top right inset).

bare SnO_2. The resistance decreased gradually with increasing temperature and was $3\,k\Omega$ at $80\,°C$. The resistance increased upon exposure to oxygen, and showed a good response to the changing oxygen concentration (0.5–5.0%).

The CCD-SCD and PXRD analyses of the Sn spheres produced by the anaerobic ethanol oxidation reaction were obtained in Fig. 4. The very sharp XRD patterns matched those of tetragonal Sn (JCPDS 04-0673)[58,62–64]. The diffraction image (inset in Fig. 4) showed single and polycrystalline natures of Sn spheres. Various crystal patterns of Phi 360 degrees obtained for other Sn spheres are provided in the Supporting Information (Fig. S7).

The reaction products produced during the aerobic and anaerobic ethanol oxidation reactions at different temperatures were examined by temperature-programmed mass spectrometry, as shown in Fig. 5. The quantity of reaction products was not measured, and only the chemical species are discussed. Under aerobic conditions, the mass signals commonly began to increase at ~250 °C, and the intensities kept increasing with in temperature. Based on the mass profiles, the oxidation gas products include hydrogen (H_2), water (H_2O), carbon dioxide (CO_2), carbon monoxide (CO), aldehyde, (CH_3CHO), methane (CH_4), acetaldehyde (CH_3CHO), and ethylacetate ($CH_3COOCH_2CH_3$, EA) with no acetic acid (CH_3COOH). On the basis of the literatures[69–71] and the present results, we propose the following simplified mechanism.

$$CH_3CH_2O\text{–}H \rightarrow CH_3CH_2O\,(ad) + H\,(ad) \qquad (1)$$

$$CH_3CH_2O\,(ad) - SnO_2 \rightarrow CH_3CHO + H\,(ad) - SnO_2 \; \textit{hydride shift} \qquad (2)$$

$$2CH_3CHO\,(ad) \rightarrow CH_3COOCH_2CH_3 \qquad (3)$$

$$CH_3CHO\,(ad) + CH_3CH_2OH\,(ad) \rightarrow CH_3COOCH_2CH_3 + H_2 \qquad (4)$$

$$C_xH_yO_z\,(ad) + O_2 \rightarrow a\,CO + b\,CO_2 + c\,H_2O \; \textit{combustion reaction} \qquad (5)$$
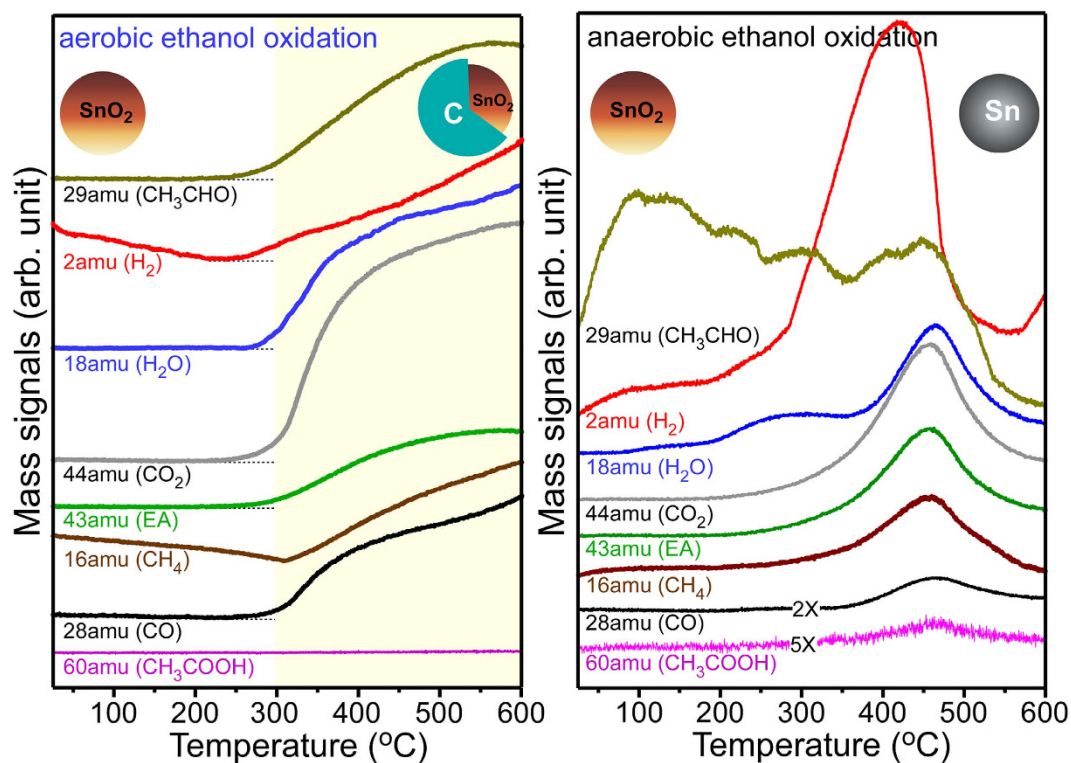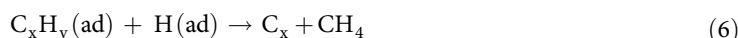
Figure 5. Mass profiles of the chemical species detected during the aerobic (left) and anaerobic (right) ethanol oxidation reactions over the SnO₂ nanoparticles. SnO₂@C core-shells were formed under aerobic conditions, whereas metallic Sn spheres were produced under anaerobic conditions.

$$C_xH_y(ad) \ + \ H(ad) \to C_x + CH_4 \tag{6}$$

In reaction (1), the O–H bond of ethanol dissociates and adsorbs as H and CH_3CH_2O. The adsorbed CH_3CH_2O desorbs as CH_3CHO (acetaldehyde) by a hydride shift reaction in (2). The acetaldehyde in (3) and (4) further proceeds to form $CH_3COOCH_2CH_3$ (ethylacetate). In reaction (5), CO, CO_2, and H_2O are formed by a combustion reaction. Elemental carbon and CH_4 are formed in reaction (6).

Under anaerobic conditions, although the reaction products were similar, the mass profile curves showed remarkable difference with temperature. Hydrogen and aldehyde were evolved earlier than the other reaction products, possibly due to $CH_3CH_2O\text{-}H \to CH_3CHO + H_2$. At above 450 °C, the mass signals (or the catalytic activity) decreased suddenly and showed the maximum intensities at approximately 450 °C. This suggests that SnO₂ changes metallic Sn at above 450 °C via the reactions of C_xH_y $(ad)-SnO_2 \to a\ CO_2 + b\ H_2O + c\ H_2 + Sn$, as discussed above. Because the reaction was performed in the absence of oxygen the oxidation of metallic Sn was less likely. Because the melting point (~230 °C)[58] of Sn is lower than the reaction temperature of ~450 °C (Fig. 5, right), the reduced Sn may form a spherical droplets of liquid Sn. Upon cooling, the liquid droplet would change to solid Sn spheres, as shown in Fig. 1. A very weak acetic acid signal was also observed under anaerobic conditions, possibly due to the reaction, $CH_3CHO + O_s \to CH_3COO(ad) + H(ad) \to CH_3COOH$, where O_s is the adsorbed oxygen species. The anaerobic ethanol oxidation reaction was also performed with 50× larger SnO₂ NPs (<100 nm) (Supporting Info. Fig. S8). Although the maximum peaks were observed at a slightly higher temperature of 500 °C, the mass profiles were similar to those of the reactions with 2 nm SnO₂ NPs. metallic Sn spheres were also obtained after the anaerobic ethanol oxidation reaction with the larger NPs.

In industry, metallic Sn is commonly produced from SnO₂ via a carbothermal reaction $(SnO_2 + C \to Sn + CO_2)$ at temperatures above 1200 °C, where carbon is used as the reducing agent. As a green method, a hydrogen reduction $[SnO_2 + 2H_2\ (g) \to Sn\ (s, l) + 2H_2O\ (g)]$ method is used at high hydrogen pressures (>30 kPa) and temperature (>700 °C)[72]. Zhang *et al.* prepared metal Sn nanobelts from SnO₂ by a substitution reaction using Zn powders in a furnace temperature of 1200 °C[73]. Compared to these two methods, the present anaerobic ethanol oxidation reaction requires a much lower temperature under ambient pressure.

To demonstrate the changes in morphology and crystal phase, another chemical reaction over the NPs was also tested, e.g., aerobic and anaerobic CO oxidation reactions. CO initially adsorbs on the oxide surface, then reacts with surface oxygen and desorbs as CO_2 (g). The surface oxygen vacancy
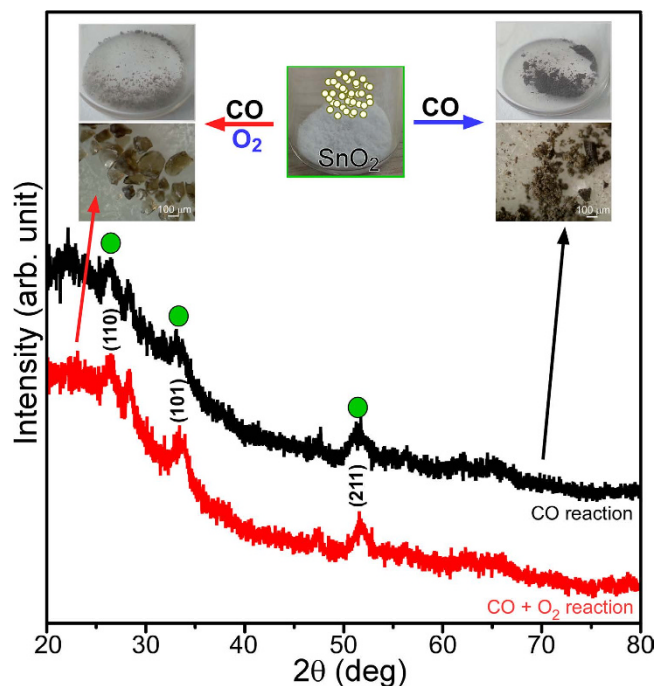
Figure 6. XRD profiles of SnO₂ after the anaerobic (5% CO in N₂) and aerobic (1% CO + 2.5% O2 in N₂) CO oxidation reactions. The inset shows photographs and optical microscopy images of SnO₂ (brown semitransparent crystals and clusters) by the aerobic (left) and anaerobic (right) CO oxidation reactions. The as-prepared SnO₂ nanoparticles (white in color) are shown in the middle.

is replenished by the adsorption of residual (molecular) oxygen; CO (g) $+$ Sn-$O_s \rightarrow CO_2$ (g) $+$ Sn-$\square_{vac}$ Sn-$\square_{vac} + 1/2O_2$ (g) $\rightarrow$ Sn-O_s, where Sn-$\square_{vac}$ = oxygen vacancy and Sn-O_s = surface oxygen species[15]. The morphology and/or crystal structure is expected to change differently according to whether there is sufficient replenishment of surface oxygen. Figure 6 shows the XRD patterns and corresponding photographs and optical microscopy images. The color and morphology showed significant changes. Larger brown semitransparent crystals appeared to be formed under aerobic conditions, whereas the aggregated power form was formed under anaerobic conditions. The corresponding SEM images are provided in the Supporting Information Fig. S9. The corresponding XRD peaks became very weak, indicating poor crystallinity, but still showed the reflection planes of tetragonal SnO₂.

Figure 7 displays the CO conversion (to CO_2) profiles of the aerobic and anaerobic CO oxidation reactions. For the first CO oxidation run under aerobic conditions, the oxidation onset temperature and $T_{10\%}$ were observed at 230 °C and 300 °C, respectively. This study showed that the SnO₂ NPs have comparable CO oxidation activity to that reported in the literature[55]. Compared to the first run, the reaction temperatures in the second run were the same between CO conversion of 0% and 20%. Above 20%, however, the conversion differed according to the reaction temperature. This suggests that the CO conversion is critically affected by heat and/or mass transfer limitations at a higher temperatures[74,75]. The CO conversion was lower for the second run at higher temperatures. At 600 °C, the catalytic activity was degraded by approximately 30% compared to that of the first run. The degraded activity was attributed to the change in surface area and crystallinity, based on the microscopy images and the XRD patterns. An activation energy (E_a) of 104.7 kJ/mol was obtained in the CO conversion range of 10–15% from the Arrhenius plot (Supporting Info. Fig. S10). Under anaerobic conditions, CO conversion (%) was much lower than that under aerobic conditions, as expected. The conversion efficiency was more degraded in the second run. Compared to the anaerobic ethanol oxidation, the CO oxidation showed no critical change in crystal phase. This suggests that CO is not a good reducing agent for SnO₂. A water signal was also detected during the first runs for both the aerobic and anaerobic reactions (Supporting Info. Fig. S11), but not during the second runs. This was expected because the as-prepared SnO₂ NPs contain water (based on the FT-IR spectrum). For the weaker water signal during the aerobic reaction, it was assumed that SnO₂ was dehydrated by a stream of oxygen before running the CO oxidation.

The BET surface area was measured to be 81.2 m²/g after anaerobic CO oxidation. The surface area was decreased to 70.0 m²/g after aerobic CO oxidation reaction. We measured a surface area of 92.5 m²/g for SnO₂@C core-shells formed after aerobic ethanol oxidation reaction. Compared with the surface area of 197. 5 m²/g for the as-prepared SnO₂ NPs, the substantial decrease is due to an increase in particle size. Energy dispersive X-ray (EDX) analysis was performed for SnO₂ NPs after the anaerobic and aerobic CO and ethanol oxidation reactions (Supporting Info. Fig. S12). For metallic Sn formed after anaerobic
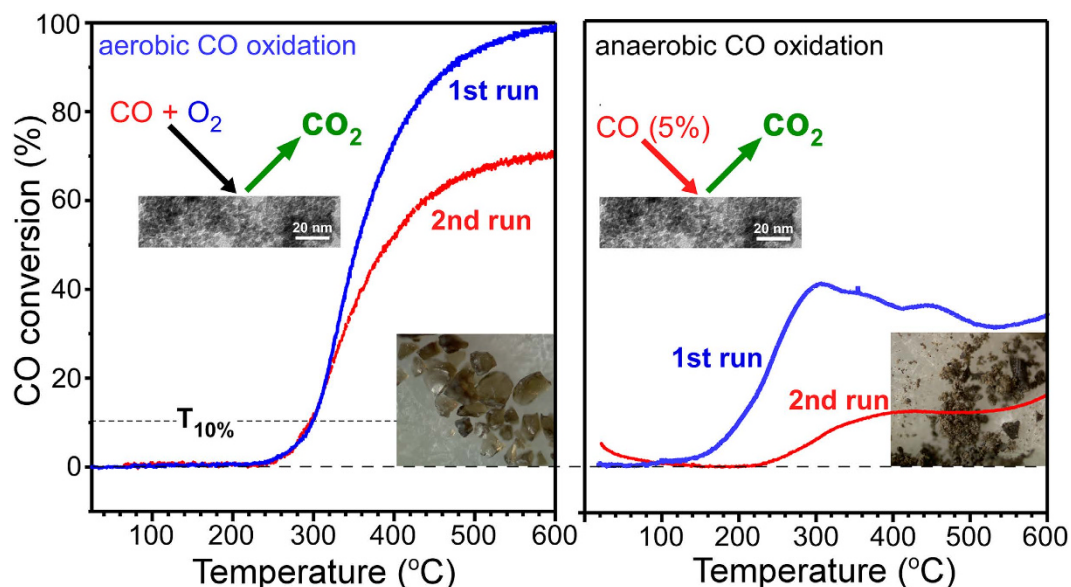
Figure 7. First and second runs temperature programmed CO oxidation conversion (%) profiles of the aerobic (left) and anaerobic (right) CO oxidation reactions over SnO_2 nanoparticles, where CO conversion (%) = {([CO]$_{in}$-[CO]$_{out}$)/[CO]$_{in}$} × 100, $T_{10\%}$ = the temperature at 10% CO conversion. CO (1%)/O_2 (2.5%) in N_2 and 5% O_2 in N_2 were used for the aerobic and anaerobic CO oxidation reactions, respectively.

ethanol oxidation, the EDX spectrum showed mainly Sn with minor impurity C signal. For SnO_2@C core-shells formed after aerobic ethanol oxidation, significant C, O and Sn EDX signals were observed as we expected. For the two samples after CO oxidation reactions, the EDX spectra showed similar Sn and O signals, but the sample after anaerobic CO oxidation showed a presence of carbon.

Raman spectroscopy was further employed to examine the structural and chemical states displayed in Fig. 8. For tetragonal SnO_2 with a space group of D_{4h}, the vibrational modes were ascribed to $1A_{1g} + 1A_{2g} + 1A_{2u} + 1B_{1g} + 1B_{2g} + 2B_{1u} + 1E_g + 3E_u$, where A_{1g}, B_{1g}, B_{2g}, and E_g are Raman active modes[15]. For the as-prepared SnO_2 NPs, three peaks were found at 467, 630 and 772 cm^{-1}, assigned to E_g, A_{1g} and B_{2g} vibrational modes, respectively. Interestingly, a broad and strong peak was observed at 569 cm^{-1}, which was attributed to surface-related defects[15,76]. The peak has commonly been observed and well known to increase with decreasing particle size[4,5,15,44]. Upon anaerobic CO oxidation, the peaks were substantially decreased and showed no clear vibrational modes, indicating formation of very poor crystalline structure. However, after aerobic CO oxidation reaction the A_{1g} peak was more clearly observed as generally expected for SnO_2 NPs[15,44]. Upon anaerobic ethanol oxidation, no Raman signal was observed, in good consistent with the literature for metallic Sn[77]. For SnO_2@C core-shells formed after aerobic ethanol oxidation, new strong Raman signals was observed, attributed to the shell-carbon species. The smaller peaks at 467 and 630 cm^{-1} were attributed to the E_g and A_{1g} vibrational modes of the core SnO_2, respectively.

Conclusion

Metallic Sn spheres can be produced by a simple anaerobic ethanol oxidation reaction over SnO_2 (2 nm size, BET surface area = 197.5 m^2/g, band gap = 3.4 eV, and broad photoluminescence peaks between 350 and 600 nm) NPs. The conversion ($SnO_2 \rightarrow$ Sn) reaction temperature was ~450 °C, which is significantly lower than the reaction temperature (1200 °C) of carbothermal Sn production used in industry. The ethanol oxidation products included H_2, H_2O, CO, CO_2, CH_4, aldehyde, and ethylacetate. On the other hand, uniform nanosized SnO_2@C core-shells could be prepared by aerobic ethanol oxidation reaction over SnO_2 NPs. The carbon overlayer was estimated to be ~1 nm on <10 nm size SnO_2 nanoparticles based on TEM. The core-shell structure showed a good oxygen sensing response and potential applicability to a gas sensor. Under aerobic conditions, the CO oxidation activity of the SnO_2 NPs showed $T_{10\%}$ = 300 °C. This suggests that SnO_2 NPs have potential applications to an oxidation catalyst.

Overall, the aerobic and anaerobic oxidation reaction could be a versatile method for the fabrication of various nanostructures and provide new insights for understanding the sensing and catalytic reaction mechanism. Uniform nanosized SnO_2@C core-shells are produced in a much simpler manner and the carbon-support material has very high potential applicability to electrode and sensor materials. The transformation from SnO_2 to metallic Sn under anaerobic conditions provides a new insights to better understanding the alcohol sensing mechanism. In addition, the unique anaerobic ethanol (alcohol) oxidation reaction could be a promising method for the industrial production of high quality metallic Sn from SnO_2.
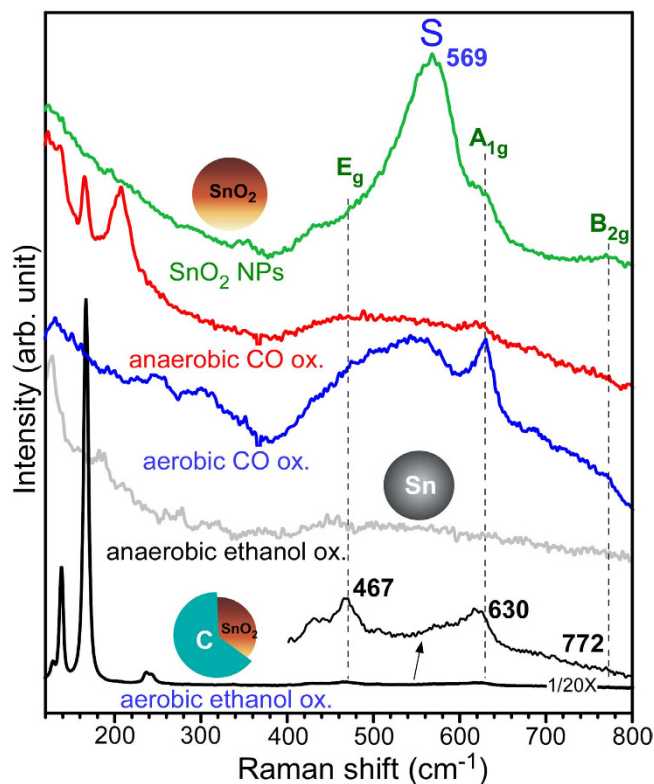
Figure 8. **Raman spectra of SnO_2 NPs before and after the anaerobic and aerobic CO and ethanol oxidation reactions.** A laser intensity of 0.25 mW was used for SnO_2@C core-shells, and 5 mW was used for other samples.

References

1. Wang, H. & Rogach, A. L. Hierarchical SnO_2 Nanostructures: Recent Advances in Design, Synthesis, and Applications. *Chem. Mater.* **26,** 123−133 (2014).
2. Kar, A. & Patra, A. Recent development of core–shell SnO_2 nanostructures and their potential applications. *J. Mater. Chem. C* **2,** 6706–6722 (2014).
3. Chen J. S. & Lou, X. W. SnO_2-Based Nanomaterials: Synthesis and Application in Lithium-Ion Batteries. *Small* **9,** 1877–1893 (2013).
4. Cheng, B., Russell, J. M., Shi, W., Zhang, L. & Samulski, E. T. Large-Scale, Solution-Phase Growth of Single-Crystalline SnO_2 Nanorods. *J. Am. Chem. Soc.* **126,** 5972–5973 (2004).
5. Xi, G. & Ye, J. Ultrathin SnO_2 Nanorods: Template- and Surfactant-Free Solution Phase Synthesis, Growth Mechanism, Optical, Gas-Sensing, and Surface Adsorption Properties. *Inorg. Chem.* **49,** 2302–2309 (2010).
6. Zhuang, Z., Huang, F., Lin, Z. & Zhang, H. Aggregation-Induced Fast Crystal Growth of SnO_2 Nanocrystals. *J. Am. Chem. Soc.* **134,** 16228−16234 (2012).
7. Wu, J. *et al.* Mechanistic Insights into Formation of SnO_2 Nanotubes: Asynchronous Decomposition of Poly(vinylpyrrolidone) in Electrospun Fibers during Calcining Process. *Langmuir* **30,** 11183–11189 (2014).
8. Jiang, L. *et al.* Size-Controllable Synthesis of Monodispersed SnO_2 Nanoparticles and Application in Electrocatalysts. *J. Phys. Chem. B* **109,** 8774–8778 (2005).
9. Ye, J., Zhang, H., Yang R., Li, X. & Qi, L. Morphology-Controlled Synthesis of SnO_2 Nanotubes by Using 1D Silica Mesostructures as Sacrificial Templates and Their Applications in Lithium-Ion Batteries. *Small* **6,** 296–306 (2010).
10. Sain, S., Kar, A., Patra, A. & Pradhan. S. K. Structural interpretation of SnO_2 nanocrystals of different morphologies synthesized by microwave irradiation and hydrothermal methods. *CrystEngComm* **16,** 1079–1090 (2014).
11. Ding, S. *et al.* Formation of SnO_2 Hollow Nanospheres inside Mesoporous Silica Nanoreactors. *J. Am. Chem. Soc.* **133,** 21–23 (2011).
12. Wang, C. *et al.* Ultrathin SnO_2 Nanosheets: Oriented Attachment Mechanism, Nonstoichiometric Defects, and Enhanced Lithium-Ion Battery Performances. *J. Phys. Chem. C* **116,** 4000–4011 (2012).
13. Tian, W. *et al.* Flexible SnO_2 hollow nanosphere film based high-performance ultraviolet photodetector. *Chem. Commun.* **49,** 3739–3741 (2013).
14. Hu, D. *et al.* Novel Mixed Phase SnO_2 Nanorods Assembled with SnO_2 Nanocrystals for Enhancing Gas-Sensing Performance toward Isopropanol Gas. *J. Phys. Chem. C* **118,** 9832–9840 (2014).
15. Sohn, Y. Structural/Optical Properties and CO Oxidation Activities of SnO_2 Nanostructures. *J. Am. Cer. Soc.* **97,** 1303–1310 (2014).
16. Choi, Y. I. & Sohn, Y. Photoluminescence profile mapping of Eu (III) and Tb (III → IV)-embedded in quantum size SnO_2 nanoparticles. *RSC. Adv.* **4,** 31155–31161 (2014).
17. Liang, J. *et al.* Bowl-like SnO_2@Carbon Hollow Particles as an Advanced Anode Material for Lithium-Ion Batteries. *Angew. Chem.* **126,** 1–6 (2014).
18. Choi, S. H. & Kang, Y. C. Kilogram-Scale Production of SnO_2 Yolk–Shell Powders by a Spray-Drying Process Using Dextrin as Carbon Source and Drying Additive. *Chem. Eur. J.* **20,** 5835–5839 (2014).

19. Zhang, L., Zhang, G., Wu, H. B., Yu, L. & Lou, X. W. Hierarchical Tubular Structures Constructed by Carbon-Coated SnO$_2$ Nanoplates for Highly Reversible Lithium Storage. *Adv. Mater.* **25**, 2589–2593 (2013).

20. Lin, Y.-S., Duh, J.-G. & Hung, M.-H. Shell-by-Shell Synthesis and Applications of Carbon-Coated SnO$_2$ Hollow Nanospheres in Lithium-Ion Battery. *J. Phys. Chem. C* **114**, 13136–13141 (2010).

21. Lou, X. W., Chen, J. S., Chen, P. & Archer, L. A. One-Pot Synthesis of Carbon-Coated SnO$_2$ Nanocolloids with Improved Reversible Lithium Storage Properties. *Chem. Mater.* **21**, 2868–2874 (2009).

22. Wang, Y., Su, F., Lee, J. Y. & Zhao, X. S. Crystalline Carbon Hollow Spheres, Crystalline Carbon-SnO$_2$ Hollow Spheres, and Crystalline SnO$_2$ Hollow Spheres: Synthesis and Performance in Reversible Li-Ion Storage. *Chem. Mater.* **18**, 1347–1353 (2006).

23. Lou, X. W., Wang, Y., Yuan, C., Lee, J. Y. & Archer, L. A. Template-Free Synthesis of SnO$_2$ Hollow Nanostructures with High Lithium Storage Capacity. *Adv. Mater.* **18**, 2325–2329 (2006).

24. Liu, Z. *et al.* Ultrafast and scalable laser liquid synthesis of tin oxide nanotubes and its application in lithium ion batteries. *Nanoscale*, **6**, 5853–5858 (2014).

25. Wang, C. *et al.* Large-Scale Synthesis of SnO$_2$ Nanosheets with High Lithium Storage Capacity. *J. Am. Chem. Soc.* **132**, 46–47 (2010).

26. Wang, Z., Luan, D., Boey, F. Y. C. & Lou, X. W. Fast Formation of SnO$_2$ Nanoboxes with Enhanced Lithium Storage Capability. *J. Am. Chem. Soc.* **133**, 4738–4741 (2011).

27. Gao, G., Wu, H. B., Ding, S. & Lou, X. W. Preparation of Carbon-Coated NiCo$_2$O$_4$@SnO$_2$ Hetero-nanostructures and Their Reversible Lithium Storage Properties. *Small* doi: 10.1002/smll.201400152 (2014).

28. Kravchyk, K. *et al.* Monodisperse and Inorganically Capped Sn and Sn/ SnO$_2$ Nanocrystals for High-Performance Li-Ion Battery Anodes. *J. Am. Chem. Soc.* **135**, 4199–4202 (2013).

29. Deng, J. *et al.* Sandwich-Stacked SnO$_2$/Cu Hybrid Nanosheets as Multichannel Anodes for Lithium Ion Batteries. *ACS Nano* **7**, 6948–6954 (2013).

30. Lin, J. *et al.* Graphene Nanoribbon and Nanostructured SnO$_2$ Composite Anodes for Lithium Ion Batteries. *ACS Nano* **7**, 6001–6006 (2013).

31. Guan, C. *et al.* Highly Stable and Reversible Lithium Storage in SnO$_2$ Nanowires Surface Coated with a Uniform Hollow Shell by Atomic Layer Deposition. *Nano Lett.* **14**, 4852–4858 (2014).

32. D'Arienzo, M., Cristofori, D., Scotti, R. & Morazzoni, F. New Insights into the SnO$_2$ Sensing Mechanism Based on the Properties of Shape Controlled Tin Oxide Nanoparticles. *Chem. Mater.* **25**, 3675–3686 (2013).

33. Zhang, S. *et al.* Facile Fabrication of a Well-Ordered Porous Cu-Doped SnO$_2$ Thin Film for H$_2$S Sensing. *ACS Appl. Mater. Interfaces* **6**, 14975–14980 (2014).

34. Li, K.-M., Li, Y.–J., Lu, M.-Y., Kuo, C. I. & Chen, L.-J. Direct Conversion of Single-Layer SnO Nanoplates to Multi-Layer SnO$_2$ Nanoplates with Enhanced Ethanol Sensing Properties. *Adv. Funct. Mater.* **19**, 2453–2456 (2009).

35. Wang, H. *et al.* Preparation of Flower-like SnO$_2$ Nanostructures and Their Applications in Gas-Sensing and Lithium Storage. *Cryst. Growth Des.* **11**, 2942–2947 (2011).

36. Wang, X. *et al.* Aligned Epitaxial SnO$_2$ Nanowires on Sapphire: Growth and Device Applications. *Nano Lett.* **14**, 3014−3022 (2014).

37. Her, Y. -C., Yeh, B.-Y. & Huang, S.-L. Vapor–Solid Growth of p-Te/n-SnO$_2$ Hierarchical Heterostructures and Their Enhanced Room-Temperature Gas Sensing Properties. *ACS Appl. Mater. Interfaces* **6**, 9150–9159 (2014).

38. Gyger, F., Hubner, M., Feldmann, C., Barsan, N. & Weimar, U. Nanoscale SnO$_2$ Hollow Spheres and Their Application as a Gas-Sensing Material. *Chem. Mater.* **22**, 4821–4827 (2010).

39. Kadir, R. A. *et al.* Electrospun Granular Hollow SnO$_2$ Nanofibers Hydrogen Gas Sensors Operating at Low Temperatures. *J. Phys. Chem. C* **118**, 3129−3139 (2014).

40. Russo, P. A. *et al.* Room-Temperature Hydrogen Sensing with Heteronanostructures Based on Reduced Graphene Oxide and Tin Oxide. *Angew. Chem. Int. Ed.* **51**, 11053–11057 (2012).

41. Suematsu, K. *et al.* Nanoparticle Cluster Gas Sensor: Controlled Clustering of SnO$_2$ Nanoparticles for Highly Sensitive Toluene Detection. *ACS Appl. Mater. Interfaces* **6**, 5319−5326 (2014).

42. She, G. *et al.* Electrochemical Sensors: SnO$_2$ Nanoparticle-Coated ZnO Nanotube Arrays for High-Performance Electrochemical Sensors. *Small* **10**, 4685–1692 (2014).

43. Kolmakov, A., Zhang, Y., Cheng, G. & Moskovits, M. Detection of CO and O$_2$ Using Tin Oxide Nanowire Sensors. *Adv. Mater.* **15**, 997–1000 (2003).

44. Jiang, C., Zhang, G., Wu, Y., Li, L. & Shi, K. Facile synthesis of SnO$_2$ nanocrystalline tubes by electrospinning and their fast response and high sensitivity to NO$_x$ at room temperature. *Cryst Eng Comm* **14**, 2739–2747 (2012).

45. Epifani, M. *et al.* The Role of Surface Oxygen Vacancies in the NO$_2$ Sensing Properties of SnO$_2$ Nanocrystals. *J. Phys. Chem. C* **112**, 19540–19546 (2008).

46. Xu, X., Zhuang, J. & Wang, X. SnO$_2$ quantum dots and quantum wires: controllable synthesis, self-assembled 2D architectures, and gas-sensing properties. *J. Am. Chem. Soc.* **130**, 12527–12535 (2008).

47. Chen, X. *et al.* Templating Synthesis of SnO$_2$ Nanotubes Loaded with Ag$_2$O Nanoparticles and Their Enhanced Gas Sensing Properties. *Adv. Funct. Mater.* **21**, 2049–2056 (2011).

48. Gubbala, S. *et al.* Surface properties of SnO$_2$ nanowires for enhanced performance with dye-sensitized solar cells. *Energy Environ. Sci.* **2**, 1302–1309 (2009).

49. Wang, Y. *et al.* Microwave-Assisted Synthesis of SnO$_2$ Nanosheets Photoanodes for Dye-Sensitized Solar Cells. *J. Phys. Chem. C* **118**, 25931–25938 (2014).

50. Dong, Z. *et al.* Quintuple-Shelled SnO$_2$ Hollow Microspheres with Superior Light Scattering for High-Performance Dye-Sensitized Solar Cells. *Adv. Mater.* **26**, 905–909 (2014).

51. Snaith, H. J. & Ducati, C. SnO$_2$-Based Dye-Sensitized Hybrid Solar Cells Exhibiting Near Unity Absorbed Photon-to-Electron Conversion Efficiency. *Nano Lett.* **10**, 1259–1265 (2010).

52. Liu, S. *et al.* Porous Fluorinated SnO$_2$ Hollow Nanospheres: Transformative Self-assembly and Photocatalytic Inactivation of Bacteria. *ACS Appl. Mater. Interfaces* **6**, 2407−2414 (2014).

53. Xia, W. *et al.* High-efficiency photocatalytic activity of type II SnO/Sn$_3$O$_4$ heterostructures via interfacial charge transfer. *Cryst Eng Comm* **16**, 6841–6847 (2014).

54. You, H. *et al.* Gold nanoparticle doped hollow SnO$_2$ supersymmetric nanostructures for improved photocatalysis. *J. Mater. Chem. A* **1**, 4097–4104 (2013).

55. Wang, X., Xiao, L., Peng, H., Liu, W. & Xu, X. SnO$_2$ nano-rods with superior CO oxidation performance. *J. Mater. Chem. A* **2**, 5616–5619 (2014).

56. Lu, Z. *et al.* Direct CO oxidation by lattice oxygen on the SnO$_2$ (110) surface: a DFT study. *Phys. Chem. Chem. Phys.* **16**, 12488–12494 (2014).

57. Du, W. *et al.* Platinum-Tin Oxide Core–Shell Catalysts for Efficient Electro-Oxidation of Ethanol. *J. Am. Chem. Soc.* **136**, 10862–10865 (2014).

58. Jeong, S., McDowell, M. T. & Cui, Y. Low-Temperature Self-Catalytic Growth of Tin Oxide Nanocones over Large Areas. *ACS Nano* **5,** 5800–5807 (2011).

59. Müller, R. *et al.* Influence of Precursor Chemistry on Morphology and Composition of CVD-Grown SnO₂ Nanowires. *Chem. Mater.* **24,** 4028–4035 (2012).

60. Li, Y. *et al.* Synthesis of self-assembled 3D hollow microspheres of SnO₂ with an enhanced gas sensing performance. *Appl. Surf. Sci.* **285P,** 130–135 (2013).

61. Zhao, Q. *et al.* Morphology-modulation of SnO₂ Hierarchical Architectures by Zn Doping for Glycol Gas Sensing and Photocatalytic Applications. *Sci. Rep.* **5,** 7874, doi: 10.1038/srep07874 (2015).

62. Alaf, M., Gultekin, D. & Akbulut, H. Electrochemical properties of free-standing Sn/SnO₂/multi-walled carbon nano tube anode papers for Li-ion batteries. *Appl. Surf. Sci.* **275,** 244–251 (2013).

63. Uysal, M., Cetinkaya, T., Alp, A. & Akbulut, H. Production of Sn/MWCNT nanocomposite anodes by pulse electrodeposition for Li-ion batteries. *Appl. Surf. Sci.* **290,** 6–12 (2014).

64. Alaf, M. & Akbulut, H. Electrochemical energy storage behavior of Sn/SnO₂ double phase nanocomposite anodes produced on the multiwalled carbon nanotube buckypapers for lithium-ion batteries. *J. Power Sources* **247,** 692–702 (2014).

65. Kar, A., Kundu, S. & Patra, A. Surface Defect-Related Luminescence Properties of SnO₂ Nanorods and Nanoparticles. *J. Phys. Chem. C* **115,** 118–124 (2011).

66. Fang, M., Tan, X., Cheng, B. & Zhang, L. SnO₂ hierarchical nanostructure and its strong narrow-band photoluminescence. *J. Mater. Chem.* **19,** 1320–1324 (2009).

67. Sohn, Y. Interfacial electronic structure and ion beam induced effect of anatase TiO₂ surface modified by Pd nanoparticles. *Appl. Surf. Sci.* **257,** 1692–1697 (2010).

68. Powell C. J & Jablonski, A. NIST Electron Inelastic-Mean-Free-Path *Database - Version 1.2, National Institute of Standards and Technology, Gaithersburg, MD* (2010).

69. Abad, A., Concepcion, P., Corma, A. & Garcia, H. A Collaborative Effect between Gold and a Support Induces the Selective Oxidation of Alcohols. *Angew. Chem. Int. Ed.* **44,** 4066–4069 (2005).

70. Guzman, J., Carrettin, S. & Corma, A. Spectroscopic evidence for the supply of reactive oxygen during CO oxidation catalyzed by gold supported on nanocrystalline CeO₂. *J. Am. Chem. Soc.* **127,** 3286–3287 (2005).

71. Li, M., Wu, Z. & Overbury, S. H. Surface Structure Dependence of Selective Oxidation of Ethanol on Faceted CeO₂ Nanocrystals. *J. Catal.* **306,** 164–176 (2013).

72. Kim, B.-S., Lee, J.–C., Yoon, H.–S. & Kim, S.-K. Reduction of SnO₂ with Hydrogen. *Mater. Trans.* **52,** 1814- 1817 (2011).

73. Zhang, J. *et al.* Synthesis of metal Sn nanobelts from SnO₂ nanopowders by a substitution reaction. *Nanotechnology* **16,** 2887–2891 (2005).

74. Park, Y., Kim, S. K., Pradhan, D. & Sohn, Y. Thermal H₂-treatment effects on CO/CO₂ conversion over Pd-doped CeO₂ comparison with Au and Ag-doped CeO₂. *React. Kinet. Mech. Cat.* **113,** 85–100 (2014).

75. Park, Y., Kim, S. K., Pradhan, D. & Sohn, Y. Surface treatment effects on CO oxidation reactions over Co, Cu, and Ni-doped and codoped CeO₂ catalysts. *Chem. Eng. J.* **250,** 25–34 (2014).

76. Xu, J. *et al.* Synthesis, characterizations and improved gas-sensing performance of SnO₂ nanospike arrays. *J. Mater. Chem.* **21,** 19086–19092 (2011).

77. Sinha, A. K., Sil, A., Sasmal, A. K., Pradhan, M. & Pal, T. Synthesis of active tin: an efficient reagent for allylation reaction of carbonyl compounds. *New J. Chem.* **39,** 1685–1690 (2015).

Acknowledgements

Author Contributions

Y.S. designed the main experimental concepts and prepared the manuscript. W.J.K. mainly performed the material synthesis and oxidation experiments. S.W.L. contributed to XRD measurements and analysis.

Additional Information

Supplementary information accompanies this paper at http://www.nature.com/srep

Competing financial interests: The authors declare no competing financial interests.

How to cite this article: Kim, W. J. *et al.* Metallic Sn spheres and SnO₂@C core-shells by anaerobic and aerobic catalytic ethanol and CO oxidation reactions over SnO₂ nanoparticles. *Sci. Rep.* **5**, 13448; doi: 10.1038/srep13448 (2015).